Petroleum Science 23 (2026) 3920–3931

Contents lists available at ScienceDirect

Petroleum Science

journal homepage: www.keaipublishing.com/en/journals/petroleum-science

Original Paper

Fluid flow visualization and resistivity variations during gas-water displacement in carbonate rock: Implications for reservoir evaluation

Qiang Lai [a], Yu-Yu Wu [a], Feng Wu [b], Jiang Jia [b,*], Xing-Gang Liu [a], Yan-Shan Yu [b], Rong Yin [a], Li Shen [a]

[a] Research Institute of Exploration and Development, PetroChina Southwest Oil & Gas Field Company, Chengdu, 610041, Sichuan, China
[b] School of Geoscience and Technology, Southwest Petroleum University, Chengdu, 610500, Sichuan, China

ARTICLE INFO

Article history:
Received 30 April 2025
Received in revised form
17 December 2025
Accepted 16 March 2026
Available online 19 March 2026

Edited by Meng-Jiao Zhou

Keywords:
Carbonate rocks
Gas-water displacement
Resistivity variation
Pore structure heterogeneity
Micro-etched glass sample

ABSTRACT

Carbonate reservoirs exhibit strong pore structure heterogeneity, leading to complex electrical properties and posing challenges for fluid saturation evaluation through well logging. To clarify the influence of fluid distribution heterogeneity on resistivity responses, a micro-etched glass model replicating real pore structures based on CT scans of core samples was developed. Gold-plated strips were integrated to enable simultaneous visualization of fluid distribution and resistivity measurement. Two sets of two-phase flow experiments were conducted: gas displacing water and water displacing gas. The results show that injected fluids preferentially form dominant flow paths through large pore-throats, while small pore-throats tend to trap residual fluids. During gas displacing water, the initially preserved water in small pores maintains a conductive network, resulting in a slow increase in resistivity. As gas invades the small throats, the conductive network breaks down, leading to a sharp rise in resistivity and a two-stage characteristic response, which reduces the applicability of Archie's equation. Even at the same saturation level, different displacement methods (conductive phase displacing non-conductive phase vs. non-conductive phase displacing conductive phase) lead to significant differences in fluid distribution and resistivity behavior, indicating that pore structure and displacement history jointly influence electrical properties. Therefore, accurate evaluation of saturation in carbonate reservoirs requires comprehensive consideration of pore structure and displacement conditions, with interpretation models adjusted according to development stages (e.g., initial accumulation vs. water flooding). This study is limited by the use of a 2D model and ambient temperature and pressure conditions, which differ from the high-temperature and high-pressure conditions of actual reservoirs. Thus, the findings primarily offer qualitative insights and are not directly suitable for quantitative application.

1. Introduction

Carbonate rocks, as important oil and gas reservoirs, are widely distributed in major petroliferous basins globally, with their reserves accounting for a significant proportion of the world's total hydrocarbon resources (Yang et al., 2018; Kolawole et al., 2022). However, carbonate reservoirs exhibit unique and complex pore structures characterized by strong heterogeneity (Xu et al., 2020; Harju et al., 2023; Malki et al., 2023), posing significant challenges for the accurate characterization and evaluation of reservoir properties (Hosseini, 2016; Elkatatny et al., 2018).

In the oil and gas industry, gas-water displacement is a common and critical process that profoundly influences fluid distribution within reservoirs and changes in petrophysical responses such as resistivity (Adebayo et al., 2017; Baban et al., 2024). Jia et al. (2021) proposed that the quantity and distribution patterns of isolated water bodies in porous media affect the electric field distribution and resistivity dispersion characteristics during resistivity measurements. The traditional Archie's equation (Archie, 1942; Jia et al., 2020) demonstrates significant limitations in describing the relationship between reservoir resistivity and water saturation in strongly heterogeneous carbonate reservoirs (Guo

* Corresponding author.
E-mail address: iamjiajiang@163.com (J. Jia).
Peer review under the responsibility of China University of Petroleum (Beijing).

https://doi.org/10.1016/j.petsci.2026.03.036
1995-8226/

et al., 2023), failing to precisely reflect real-world scenarios. The Archie formula exhibits poor applicability in carbonate reservoirs, primarily due to their complex pore structure and strong heterogeneity (Al-Mahtot, 2024). In reservoirs with heterogeneous pore-throat structures, fluid behavior dominates the electrical responses (He et al., 2020; Jia et al., 2022; Mohammadi et al., 2025).

In the field of fluid dynamics in carbonate reservoirs, scholars have conducted extensive research on how pore structure regulates fluid behavior. Hosseini et al. (2024) using carbonate rock samples as study subjects, examined the significant influence of pressure and temperature on fluid migration range and spontaneous imbibition rate. Micro-etched samples are widely used in petroleum engineering for visualizing multiphase flow characteristics in porous media (Sharbatian et al., 2018; Gogoi and Gogoi, 2019; Xu et al., 2020; Qian et al., 2025), particularly in the burgeoning CCUS-EOR (carbon capture, utilization, and storage-enhanced oil recovery) field (Xu et al., 2017; Ho et al., 2021; Liang et al., 2024). Lu et al. (2021) utilized micro-etched chips to observe mass transfer processes and salt precipitation following CO_2 injection into brine-saturated porous media, discovering that CO_2 microbubbles expand in dominant flow channels, thereby impeding fluid flow. Hao et al. (2022) visualized CO_2-oil two-phase migration and miscibility processes using realistic pore-scale models, observing distinct flow stratifications under immiscible conditions. Zhang et al. (2022) conducted high-temperature, high-pressure microfluidic displacement experiments on micro-etched samples and found that subsequent CO_2 injection after waterflooding effectively reduces asphaltene deposition in crude oil.

Building upon these hydrodynamic insights, the microscopic distribution morphology within the pore space directly governs current transmission pathways and, consequently, the resistivity response characteristics of the rock (Zhang et al., 2025). A significant distinction exists between the conduction mechanisms of isolated water ganglia and continuous water films in porous media. When the aqueous phase is confined within dead-end pores or forms isolated blobs, its contribution to current transmission is effectively severed (Cai et al., 2017; Han et al., 2019). Conversely, even at low saturation conditions, continuous water films coating grain surfaces can establish effective conductive networks, causing the resistivity index to deviate significantly from classical theories (Revil et al., 2018). This microscopic heterogeneity is particularly pronounced in carbonate reservoirs, where complex pore networks—ranging from micropores to vugs-render the conventional Archie's equation insufficient for describing the non-linear relationship between resistivity and saturation, often leading to substantial biases in reservoir evaluation (Liu et al., 2018; Prakoso et al., 2025). Furthermore, during gas-water or oil-water displacement processes, the intrusion of the non-wetting phase dynamically reconstructs fluid distribution—evolving from connected networks to discrete droplets (Zhao et al., 2025a). This evolution, accompanied by contact angle hysteresis and variations in water film thickness, results in resistivity responses that exhibit strong history dependency and anisotropy (Nepal et al., 2025). Therefore, thoroughly decoupling the interactions among pore structure, wettability, and microscopic fluid configuration is critical for addressing the limitations of Archie's formula and improving the accuracy of hydrocarbon saturation interpretation.

Compared to conventional experimental methods, microscopic visualization experiments offer advantages such as precise control, real-time observation, and compact size (Wang et al., 2024). Conventional micro-etched samples differ significantly from traditional core samples, as their etched regions (representing porous media properties) are surrounded by non-conductive matrix materials like glass, making direct resistivity measurements impossible. To enable simultaneous real-time visualization of two-phase flow and resistivity measurements in porous media, gold-plated strips were added to the cover plates of micro-etched glass samples fabricated from actual carbonate rock CT images, extending to the sample edges for impedance measurements within the etched regions. By monitoring fluid distribution and impedance changes during two-phase displacement processes, this study investigates the impact of gas-water flow on the resistivity of strongly heterogeneous carbonate rocks, providing references for optimizing saturation logging evaluation methods in heterogeneous reservoirs.

2. Sample and methods

2.1. Preparation of micro-etched samples

To optically visualize the gas-water two-phase fluid distribution in the pore space of samples, two visual micro-etched samples were fabricated based on the pore-structure characteristics of real carbonate core. The visual samples enable researchers to directly observe the displacement process of the two - phase fluids in the pore space of the samples (Wu et al., 2020). When combined with resistivity measurements, it helps to understand the distribution of two-phase fluids and the laws of resistivity changes in carbonate gas reservoirs during the processes of reservoir formation and development.

Micro-etched samples are widely used in the field of petroleum engineering for the visualization research of multiphase flow. The full-diameter core selected in this article was taken from the 315.20–316.07 m depth section of Well Wang 1 in the Sichuan Basin. The rock type is dolomite. The core surface is smooth and free of obvious irregularities. The core size is 117.2 mm in diameter × 101.6 mm in length. The corresponding pore size range (360–4350 μm) of its rock electrical parameters is $a = 1.07$; $b = 0.99$; $m = 3.42$; $n = 1.55$. These four parameters are key to the Archie equation: a is the tortuosity factor, b is the formation water saturation index, m is the cementation index, and n is the saturation index.

The actual carbonate rock core CT data used in this study were obtained by using the CT scanner nanoVoxel-4000 from Tianjin Sanying Precision Instrument Co., Ltd. The maximum voltage of the instrument was 300 kV. The pixel resolution capability of this scan was 61 μm per pixel. The scan resulted in the acquisition of a three-dimensional CT data of the real carbonate rock core with a three-axis size of 1920 pixels × 1920 pixels × 1665 pixels. Based on the high-resolution CT scan images of real carbonate rock cores, representative two-dimensional CT slices were selected, and an image area of 3 cm in length and 2 cm in width was cut out (Fig. 1 (a)); the images were processed for noise removal and threshold segmentation, and the pore structure in the two-dimensional slice images was initially obtained (Fig. 1(d)) (Wang et al., 2024). The pore-throat network in micro-etched samples represents a simplified two-dimensional model (Qian et al., 2025). Considering that the throat network of real cores is complex and the true connectivity cannot be fully reflected in a two-dimensional image, artificial modifications are made to the processed image. Some long and narrow throats are added to ensure that the pores are interconnected.

Using the mercury intrusion curve data of the same core (Fig. 1(b)), the throat radius distribution (Fig. 1(e)) was obtained. In the throat radius distribution, the peak throat radius of 200 μm was found, along with the range of left and right expansion. When the left boundary and right boundary were expanded to 160 μm and 240 μm respectively, the percentage of pore volume controlled by the selected range of throat was 57% (this value just exceeded 50%), thereby determining the throat radius range to be 160–240 μm. Using the real carbonate rock core CT data, a three-dimensional image (Fig. 1(c)) was extracted, a ball-stick model

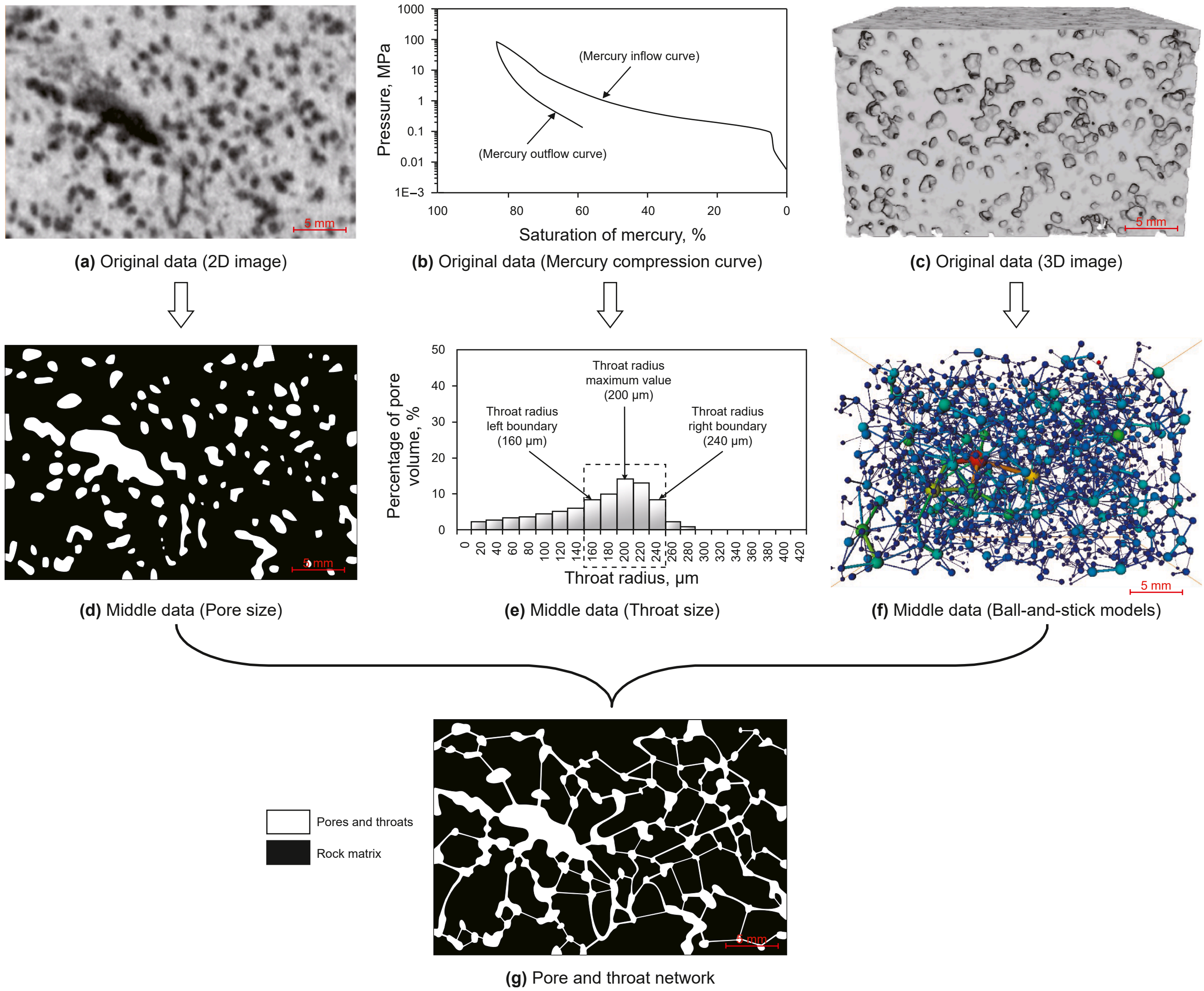

Fig. 1. The extraction process of pore and throat network.

(Fig. 1(f)) was constructed, the pore coordination number was obtained, and the main throat and their positions were determined. Finally, based on the main throat radius range of 160–240 μm determined by the mercury intrusion curve data, the main connected throats were retained, additional throats were added between appropriate pores, and the throat with a large curvature and extremely small radius was simplified. The pore structure (Fig. 1(d)) was connected to obtain the final pore-throat network (Fig. 1(g)).

The high-resolution CT scan images of the genuine carbonate rock core are shown in Fig. 2(a). And the processed binary image of the two-dimensional pore and throat network is shown in Fig. 2(b). Fluid channels and diversion areas also need to be added at both ends of the etched area. Then, an etching mask is made according to the constructed binary image of the two-dimensional pore and throat network, and the etching solution is used to corrode away the pore and throat areas that need to be hollowed out on the glass substrate. Finally, a layer of highly transparent glass cover plate is covered and bonded to form an approximately two-dimensional visual porous media model.

The resistivity of the etched area cannot be measured in traditional glass micro-etched samples. To solve this problem, as shown in Fig. 1(a), two gold-plated films are designed on the cover plate at positions corresponding to the etched area and extended to the edge of the sample before bonding the glass cover plate to the substrate, and openings are designed at the corresponding positions on the edge of the substrate. In this way, the Kelvin clips of the impedance analyzer can be used to clamp the two gold-plated films and use them as measurement electrodes to measure the resistivity of the etched area in the sample by the two-electrode method. The fabricated sample is shown in Fig. 2(c). Two samples with distinct pore structure characteristics were fabricated, featuring a pore-throat region measuring 3 cm in length, 2 cm in width, and with an etching depth of 5 μm.

2.2. Experimental system

The entire visualization experimental system is mainly composed of six parts, including: (1) Micro-etched sample: Based on transparent glass material, the pore-throat structure is carved onto the transparent material, with fluid inlets and outlets and a gold-plated film set up, which can be externally connected to fluid hoses and Kelvin clamps. (2) Constant flow injection pump: Through the fluid hose, gas or sodium chloride solution is stably

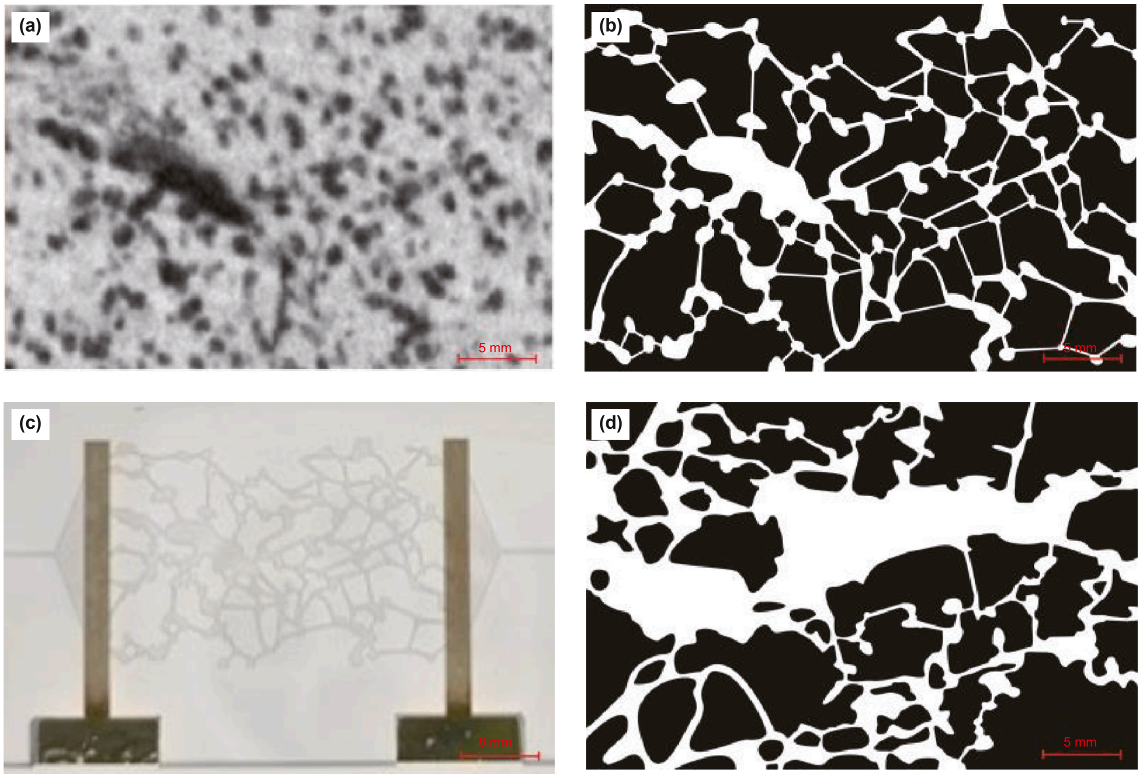

Fig. 2. Process of fabricating glass micro-etched samples based on real carbonate rock CT images. **(a)** Original core CT image for sample A; **(b)** processed binary image of the pore-throat network for sample A; **(c)** completed glass micro-etched sample A; **(d)** processed binary image of the pore-throat network for sample B.

injected into the microscopic etching sample. (3) Impedance analyzer: By connecting the microscopic etching sample with a Kelvin clamp, the impedance data is measured. (4) Microscope: Real-time capture the changes and distribution of fluid saturation within the microscopic etching sample. (5) Liquid collection beaker: Collect the fluid discharged from the microscopic etching sample. (6) Computer: Collect the impedance data measured by the impedance analyzer, record the changes and distribution of body saturation captured by the microscope, and perform image processing using ImageJ software. The structural schematic diagram and physical photos of the experimental system are shown in Fig. 3.

2.3. Experimental principle

All instruments are calibrated in advance and operated in coordination, guaranteeing the accuracy and reliability of the micro-etched glass experiments. The impedance analyzer has been calibrated regularly with high-precision impedance standard components before the experiment. The inlet of the micro-etched sample is connected to a constant-flow injection pump. Under its control, the fluid in the syringe can enter the pore-throat network in the micro-etched sample from the inlet at a constant flow rate. The outlet is connected to a beaker through a hose to collect the fluid discharged from the micro-etched sample. During the fluid displacement process, the changes and distribution of fluid saturation in the micro-etched sample are captured by a microscope and recorded by a computer. When measuring impedance data using an impedance analyzer, connect the two groups of gold-plated electrodes of the microscopic etched sample to the Kelvin clamp of the impedance analyzer. The impedance analyzer can directly output the impedance of the sample at a frequency of 1 kHz, which is a commonly used frequency in petrophysical experiments and can effectively avoid the electrode polarization effect and the polarization interference at the fluid-mineral interface (Jia et al., 2021). For each fluid saturation state, three parallel

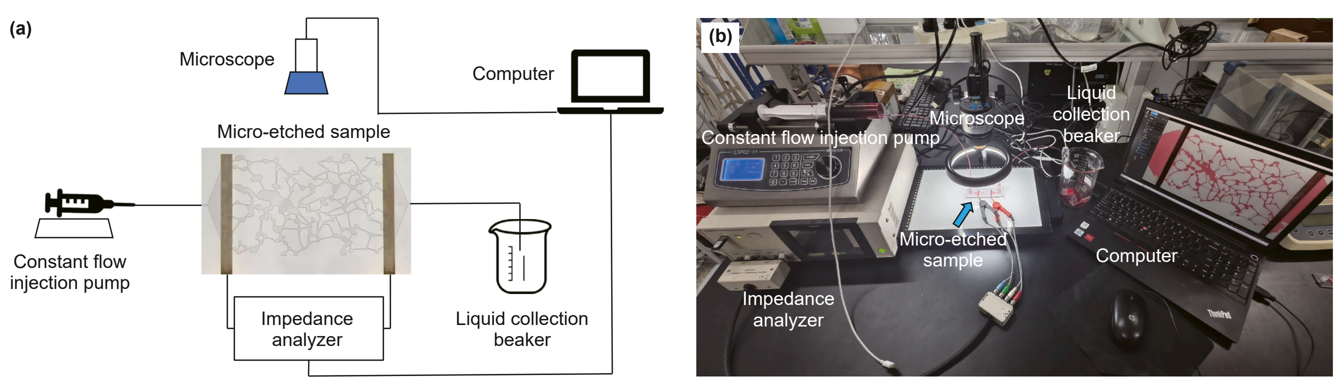

Fig. 3. The experimental system's: **(a)** principle schematic diagram and **(b)** on-site photo.

impedance measurements are performed. Only when the relative differences among the three measurement values are all less than 5%, take the arithmetic average of the three measurements as the final impedance data for this state. At this time, collect the impedance data of the sample's pore-throat area and upload it to the computer. Then, based on the size information of the sample's etching area, estimate the resistivity of this area.

During the experimental process, the displacement of gas-water two-phase fluid needs to be carried out. The aqueous phase fluid used in the experiment is a sodium chloride solution with a salinity of 150,000 ppm, and the gas - phase fluid is air. In order to better distinguish the distribution of gas-water two-phase fluids from the images, the sodium chloride solution was dyed with red ink. Threshold segmentation method is a commonly used approach for extracting image features. By selecting multiple different gray-scale thresholds, different features of the image can be separated one by one. In this experiment, there are three features: the skeleton, liquid phase, and gaseous phase fluids. Therefore, the threshold segmentation method is suitable for this case. According to the micro-etched sample photos taken by the microscope, appropriate gray - scale values are selected for image segmentation, so that the positions occupied by the skeleton, liquid phase, and gas-phase fluids in the sample can be extracted respectively (Zhao et al., 2025b). In the previous section (Fig. 1(g)), the number of pixels occupied by the pore-throat network (px_{p}) can be obtained. Based on the corresponding number of pixels (the number of liquid phase fluid pixels is px_{w}, the number of gas phase fluid pixels is px_{g}, and the number of skeleton pixels is px_{m}). Eqs. (1) and (2) can calculate the saturation of the liquid phase fluid (S_{w}) and the gas phase fluid (S_{g}):

$$S_{\mathrm{g}} = \frac{px_{\mathrm{g}}}{px_{\mathrm{p}}} \tag{1}$$

$$S_{\mathrm{w}} = \frac{px_{\mathrm{w}}}{px_{\mathrm{p}}} \tag{2}$$

where S_{g} represents the gas saturation, %; S_{w} represents the water saturation, %; px_{g} represents the number of gas-phase fluid points, dimensionless. px_{w} denotes the number of liquid-phase fluid points, dimensionless; px_{p} represents the number of pixels in the pore-throat network, dimensionless. The saturation is expressed as a percentage (%) by multiplying the pixel ratio by 100.

Finally, based on the ratio of the pixel points occupied by each component, the saturations of the liquid-phase and gas-phase fluids can be calculated. Fig. 4 shows the original photo of the sample when the water saturation is 70.54% and the distribution of each segmented component.

2.4. Experimental procedure

The experimental process is shown in Fig. 5 and can be divided into three stages in total:

(1) Full saturation of the sample: First, use a very high flow rate of 50–200 μL/min to quickly and fully saturate the pore space in the sample with a saline solution. This flow rate is 10–40 times the low flow rate (5 μL/min) used in the displacement stages, ensuring rapid filling of the pore-throat network without residual air bubbles. This process aims to simulate the formation period of the stratum. Finally, the water saturation of the sample approaches 100%. Take a photo of the fluid distribution in the sample for archiving. Corresponding to the actual geological conditions, this process generally does not involve fluid migration, so the impedance of the sample is not measured at this stage.

(2) Displace the saline solution in the pores of the sample with air at a low flow rate (5 μL/min was used in the experiment). This process simulates the process of gas reservoir formation, where natural gas migrates and accumulates in the pores of the rock. Whenever the water saturation in the pores of the sample changes, take a photo to record the fluid distribution in the sample and measure the impedance under the corresponding state. When the fluid distribution in the sample no longer changes, end the experiment of this stage. At this time, the water saturation in the sample is regarded as the irreducible water saturation.

(3) Displace the fluid in the pores of the sample with a saline solution at a low flow rate (5 μL/min was used in the experiment). This process simulates the development stage of the gas reservoir. As the natural gas is developed, the surrounding formation water or the saline solution injected for development is reinjected into the pores of the reservoir. Similarly, whenever the water saturation in the pores of the sample changes, take a photo to record the fluid distribution in the sample and measure the impedance under the corresponding state. When the fluid distribution in the sample no longer changes, end the experiment. At this time, the gas saturation in the sample is regarded as the residual gas saturation.

3. Results and analysis

3.1. Gas and water seepage law

Through micro-etched glass sample combined with a microscope, the seepage process of gas-water two-phase fluids in pores and throats can be clearly observed and recorded. Fig. 6 shows a simple process of the distribution changes of gas-water two-phase fluids in the pore-throat space of the sample A throughout the experiment.

As can be seen from Fig. 6, in the early stage of two-phase fluid displacement, the injected fluid will preferentially occupy the dominant seepage channels such as large-scale pore-throats. Once the injected fluid forms a connected fluid channel, the subsequent injected fluid will flow more easily along the already formed connected path, exhibiting an “empirical” following behavior as observed in the displacement process. And a large number of pore-throat spaces that still retain the original fluid after the injected fluid has formed a connected path will keep the original fluid unchanged (Hao et al., 2022), unless the displacement pressure is increased. This fluid following behavior is mainly influenced by the difference in capillary pressure between different paths and wettability. The throats of the channels already occupied by the displacing fluid are relatively coarser, resulting in lower capillary pressure. Furthermore, the wettability of the inner surfaces of the pore-throats in these channels is more favorable to the displacing fluid, which further reduces the flow resistance of subsequent displacing fluid along these existing paths and strengthens the following behavior.

Therefore, when using brine to displace air, the water saturation obtained at the end of the simulated sedimentation process stage (Fig. 6(d)) is higher than that obtained at the end of the simulated development stage (Fig. 6(l)). It can be inferred that the primary factors influencing natural gas recovery in pore-throat spaces are the highly connected large pore-throats. To further develop the residual gas, it is necessary to adopt waterflooding measures with higher pressure.

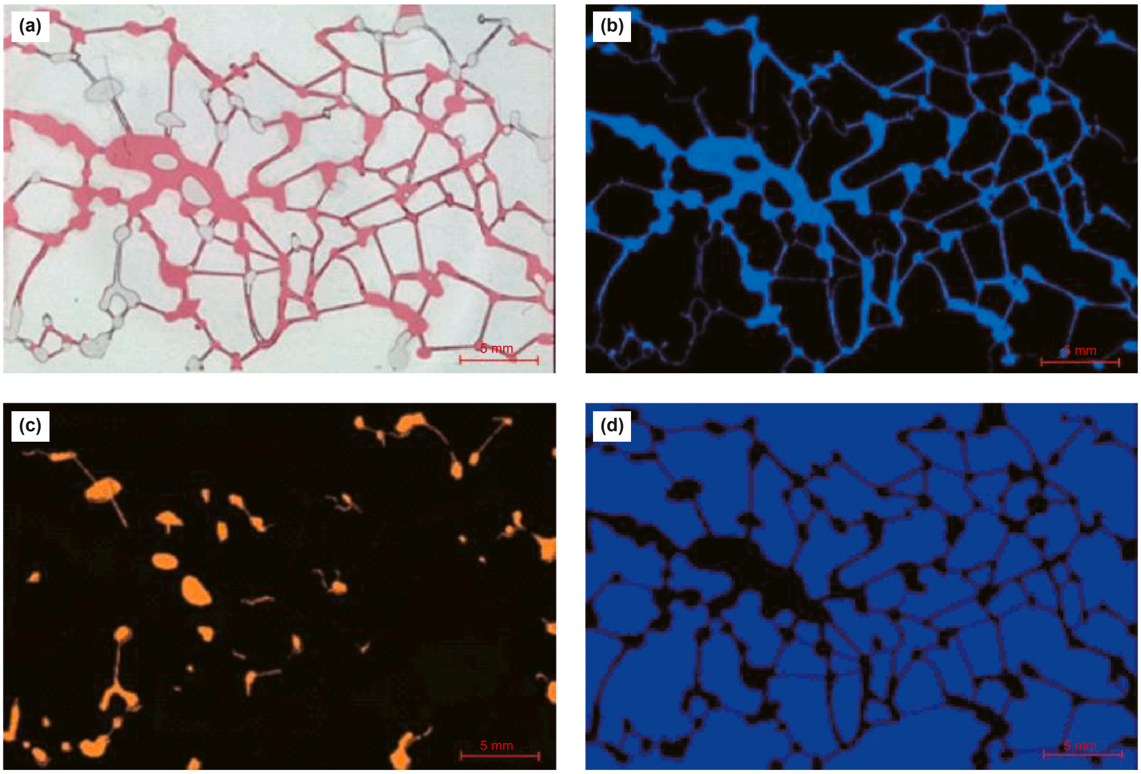

Fig. 4. Images of the sample at a water saturation of 70.5%: **(a)** Original photo; **(b)** distribution area of liquid-phase fluid (bule); **(c)** distribution area of gas-phase fluid (yellow); and **(d)** solid matrix area of the sample (bule).

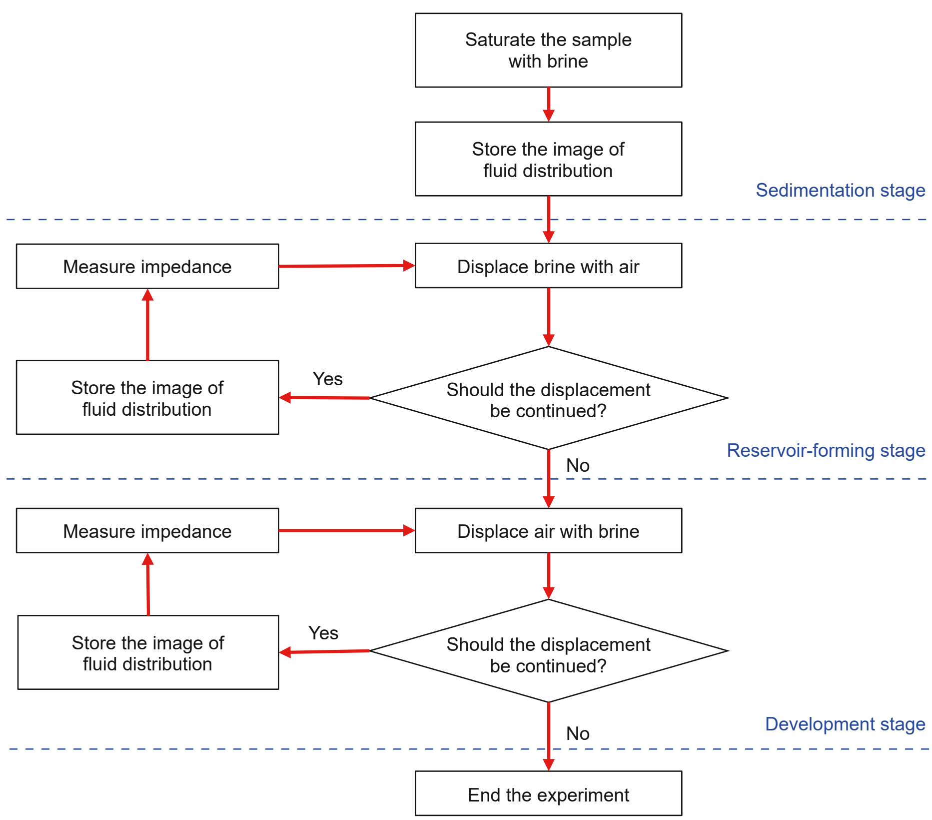

Fig. 5. Experimental flow.

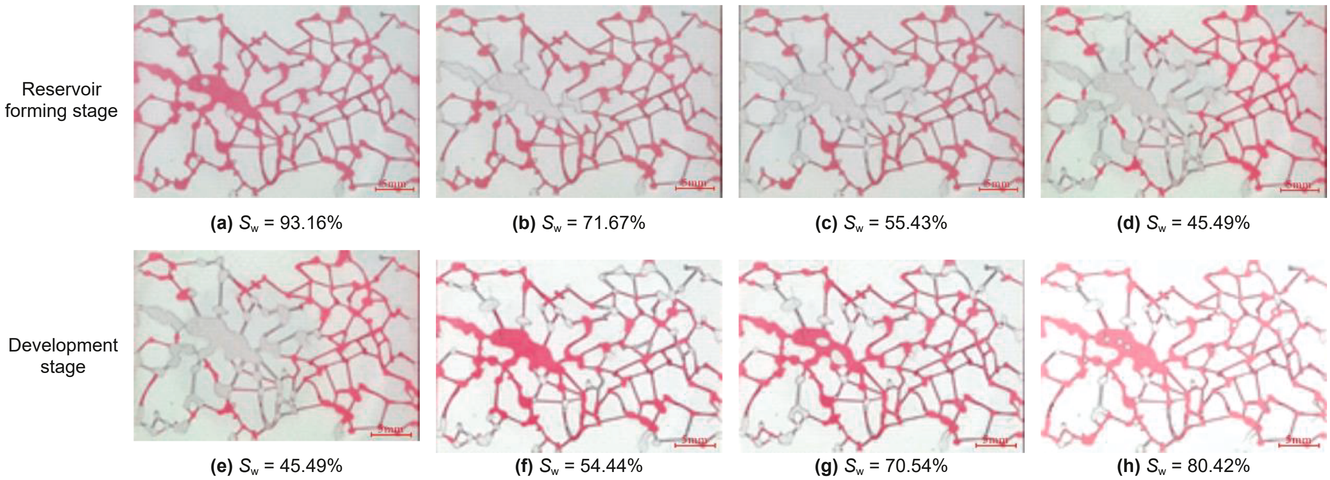

Fig. 6. Fluid distribution and changes in the pore-throat space of the sample A during the experimental process: **(a)** $S_w = 93.16\%$; **(b)** $S_w = 71.67\%$; **(c)** $S_w = 55.43\%$; **(d)** $S_w = 45.49\%$; **(e)** $S_w = 45.49\%$; **(f)** $S_w = 54.44\%$; **(g)** $S_w = 70.54\%$; **(h)** $S_w = 80.42\%$. The red part in the figure represents the brine solution. The left side of each sub-figure is the injection end of the fluid, and the right side is the outlet end of the fluid.

In the pore-throat space of heterogeneous porous media, the following pore-throat spaces are prone to trap residual fluids: (A) Pore-throat spaces where the direction of the throat is nearly perpendicular to the dominant seepage channel (indicated by the blue arrow in Fig. 7) (as shown in the red circle in Fig. 7); (B) Narrow throat spaces and small pore spaces connected to the narrow throats (as shown in the green circle in Fig. 7); (C) Relatively narrow pore-throat spaces that are in parallel with large-scale pore-throats (as shown in the light blue circle in Fig. 7); (D) In irregular pores, the “sharp corner areas” that are less disturbed by the fluid (as shown in the orange circle in Fig. 7).

Fig. 8 illustrates the evolution of two-phase fluid distribution during the experiment in sample B. Compared to sample A, sample B exhibits a more significant disparity in pore-throat sizes. A distinct, interconnected pathway composed of larger pores is observed between the injection and outlet ends. During both the gas charging and development stages, the injected fluid rapidly occupied this preferential flow path, leading to a swift decrease in the saturation of the original fluid phase. Although the narrower pore spaces, which are smaller than this dominant channel, still maintain reasonably good connectivity, they are relatively disadvantaged. This often results in the formation of trapped zones for the original fluid, as seen in the upper left corner of the sample.

Due to experimental constraints, this study did not investigate the effects of factors such as temperature, pressure, and wettability on the seepage behavior of gas-water two-phase fluids within the pore spaces of carbonate rocks (Hosseini et al., 2023). However, the optical visualization of the samples and the simultaneous resistivity measurements provided valuable support for revealing the influence of fluid distribution characteristics within the pores on the rock’s resistivity.

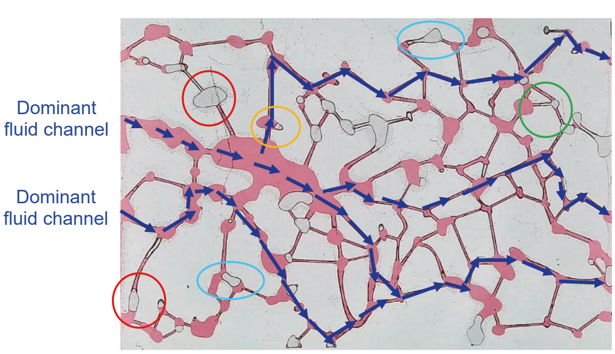

Fig. 7. The dominant fluid channel in the pore-throat space of the sample and the areas where residual fluid is likely to form.

3.2. Resistivity variation

According to Archie’s formula, generally speaking, there is a good power exponential relationship between the resistivity of the rock and the water saturation (S_W) (Jia et al., 2020):

$$\frac{R_t}{R_0} = I = \frac{b}{S_W^n} \tag{3}$$

where R_t is the resistivity of the rock, Ω.m; R_0 is the resistivity of the rock when it is fully saturated with water, Ω.m; I is the resistivity index, dimensionless; b is the water saturation index, dimensionless; and n is the saturation index, dimensionless.

Since the sample’s water saturation did not reach 100% during the experiment, the R_0 value was not directly measured. Therefore, the relationship between R_t and S_W was fitted with a power function according to Archie’s formula, and the value of R_t when $S_W = 100\%$ calculated from the fitting result was taken as R_0.

The relationship between R_t and S_W during the gas-displacing-brine and brine-displacing-gas stages for both samples is illustrated in Fig. 9. Although significant differences exist in the R_t–S_W relationships between these two stages, both follow a well-defined power-law relationship.

The resistivity-saturation relationship curve for the gas-displacing-brine process exhibits a distinct segmented characteristic. When fitting the entire dataset with a power-law function (in the form of Archie’s equation), a systematic deviation was observed between the data points and the fitting curve at high water saturation regions during the gas-displacement stage. This indicates that for our experimental core, the conductive mechanism during the initial stage of gas displacement (at high water saturation) may differ from that at lower saturation stages. Directly extrapolating data from this phase to $S_W = 100\%$ to derive R_0 would introduce significant error.

In contrast, the brine-displacing-gas process demonstrated better reproducibility and a higher degree of consistency with the power-law relationship across the entire saturation range.

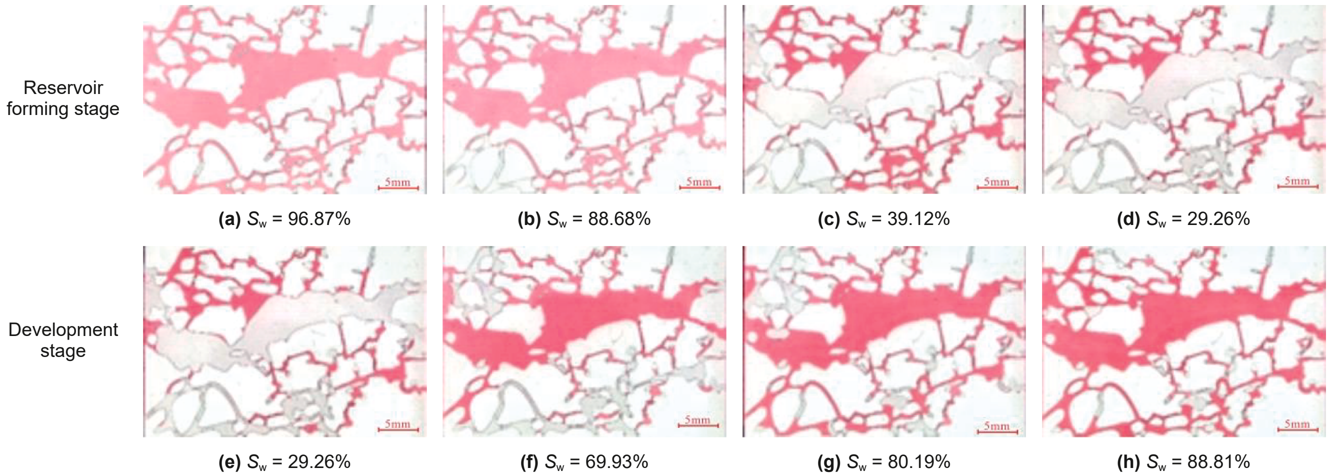

Fig. 8. Fluid distribution and changes in the pore - throat space of the sample B during the experimental process: **(a)** S_w = 96.87%; **(b)** S_w = 88.68%; **(c)** S_w = 39.12%; **(d)** S_w = 29.26%; **(e)** S_w = 29.26%; **(f)** S_w = 69.93%; **(g)** S_w = 80.19%; **(h)** S_w = 88.81%. The red part in the figure represents the brine solution. The left side of each sub-figure is the injection end of the fluid, and the right side is the outlet end of the fluid.

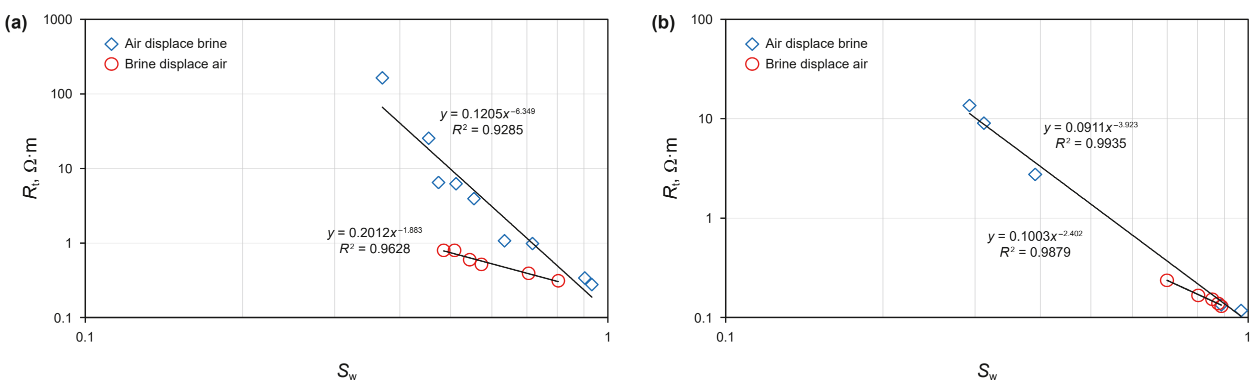

Fig. 9. The relationship between the resistivity and the water saturation during the experiment of: **(a)** sample A and **(b)** sample B.

Therefore, utilizing the fitting trend line from the "brine-displacing-gas" stage experimental data and extrapolating it to $S_W = 100\%$ to determine R_0 is a more rational and reliable approach.

Based on the fitting results, the resistivities of the two samples at 100% water saturation (R_0) were determined to be 0.2012 Ω m and 0.1003 Ω m, respectively. After establishing R_0, the resistivity indices (I) of both samples at different water saturation levels were calculated using Archie's equation, and their relationship with water saturation is plotted in Fig. 10. It should be noted that during the gas-displacing-brine process, while the water saturation in Sample A decreased to a minimum of 20.13%, the sample's impedance at this saturation level exceeded the measurement range of the impedance analyzer, preventing the acquisition of resistivity data under this condition.

Fig. 10 shows that during the gas-displacing-brine stage, as gas is injected, the water saturation gradually decreases while the resistivity index increases accordingly. However, a two-stage relationship exists between the resistivity index and water saturation. Taking sample A as an example, when the water saturation is above 0.6, the injected gas preferentially occupies the larger pores due to their lower capillary pressure. Although the overall water saturation decreases significantly, the original brine remains trapped in the smaller pore-throats, maintaining a conductive pathway connecting the injection and outlet ends (as shown in Fig. 6(b)). Consequently, the rate of increase in sample impedance and resistivity index is relatively slow.

As gas injection continues and water saturation falls below 0.6, the gas begins to invade the smaller pores and throat spaces, nearly severing the conductive pathway formed by the original brine between the injection and outlet ends (as shown in Fig. 6(c)). This leads to a sharp increase in sample impedance and the resistivity index, manifesting as a steeper slope on the log-log plot in Fig. 8.

The relationship between resistivity and water saturation for sample B during the gas-displacement stage also exhibits a two-stage characteristic. However, due to the highly efficient flow capacity of the large pore-throat channel in the center of the sample combined with its thin geometry, the water saturation dropped rapidly from high to low levels. This posed experimental challenges for reliable impedance measurement within the intermediate water saturation range (≈40%–85%), as the displacement process was difficult to pause.

The two distinct stages in the increase rate of the resistivity index with decreasing water saturation correspond to the invasion process of the non-conductive fluid phase into the large pore spaces and the small pore spaces, respectively. Based on the experimental results from sample A, the water saturation boundary between these two stages is approximately 60%, but this value

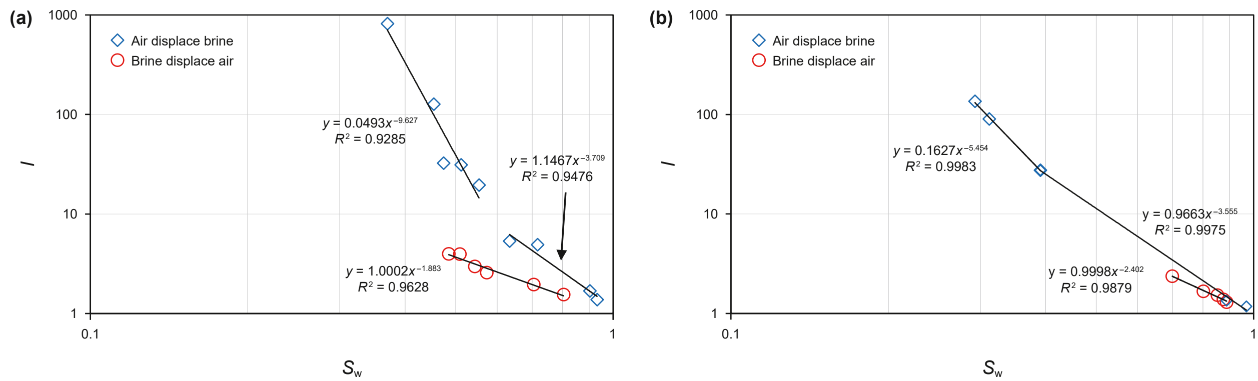

Fig. 10. The relationship between the resistivity index and water saturation during the experiment of: **(a)** sample A and **(b)** sample B.

is specific to the sample used in this experiment. It can be inferred that the magnitude of this critical water saturation value and the difference in slopes of the data in the log-log plot between the two stages are likely related to the sample's pore size distribution or the degree of pore structure heterogeneity. Further experimental studies are needed to verify these relationships.

During the brine-displacing-gas stage, as the pore space within the sample is already wetted by the liquid phase, the conductive brine solution rapidly occupies the large pore spaces at the initial stage of displacement, establishing a conductive pathway connecting the injection and outlet ends (as shown in Fig. 6(f)). Consequently, the sample's resistivity index, or resistivity, decreases sharply. As the displacement process continues, the water saturation of the sample gradually increases, and the resistivity index decreases correspondingly, showing a good linear relationship on the log-log plot.

He et al. (2020) also observed this two-stage relationship in experiments based on carbonate rock samples from the Longwangmiao Formation in the Sichuan Basin. Ara et al. (2001) discussed the validity of Archie's equation for carbonates, suggesting that the complex pore structure and wettability of carbonate rocks can lead to a segmented relationship between resistivity and water saturation. At high water saturations, conductivity primarily relies on connected pore water, while at low water saturations, the water phase becomes isolated in micropores, resulting in more tortuous conductive paths and a higher n value. The experimental results in this study provide visual, intuitive evidence for this claim.

Electrical property experiments on core samples are a common petrophysical method used in actual exploration and development to determine parameters for saturation models. Displacing conductive fluid with a non-conductive fluid (gas or oil) to vary saturation is a standard technique for adjusting saturation in these experiments (Li et al., 2019; Jia et al., 2021). Therefore, the segmented variation in rock resistivity revealed in this study should draw the attention of geophysicists.

3.3. Impact of the development process

By comparing the experimental data of the two stages in Fig. 10, it can also be found that, at similar saturations, the sample's resistivity during air-displacing-brine is consistently higher than that during brine-displacing-air. Moreover, this difference seems to be the largest when the saturation is at a moderate level.

Fig. 11 shows the fluid distribution images of the sample when the water saturation of the sample is close during the stage of air displacing brine and the stage of brine displacing air. It can be seen that although the sample has a similar water saturation in the two states, there are significant differences in the fluid distribution. During the gas displacing water stage, the non-conductive air occupies the large-scale pores and cuts off the four inlets at the fluid injection end, resulting in no conductive fluid connecting the electrodes located at the fluid injection end and the outlet end, and the resistivity of the sample is relatively high. However, during the stage of brine displacing air, the conductive fluid occupies the large-scale pores and constructs a conductive path connecting the two electrodes, and the non-conductive gas is located in the small-scale pores, so it has a relatively low resistivity. Therefore, for the same sample, using conductive fluid to displace non-conductive fluid and using non-conductive fluid to displace conductive fluid will obtain different resistivity variation laws.

Corresponding to the scale of a gas reservoir, the fluid distribution in the pores during the formation process of the gas reservoir conforms to the characteristics of non-conductive phase fluid displacing conductive phase fluid. In the late stage of gas reservoir development, when encountering water flooding or experiencing the process of water flooding development, the distribution of pore fluids conforms to the characteristics of conductive phase fluid displacing non-conductive phase fluid. Therefore, at different development stages of the gas reservoir, different model parameters need to be adopted when using Archie's formula for reservoir saturation evaluation.

Fig. 12 provides a more detailed explanation and demonstration. Well A in the figure is an exploration well drilled in the early stage of development. The reservoir has just experienced the process of reservoir formation, in which natural gas occupies the large-scale pore-throat spaces. The relationship between its resistivity index and water saturation conforms to the Archie model corresponding to the blue fitting line in the figure. With the continuous development of the gas reservoir, Development well B is added. Due to water flooding, the location where it is located has changed from a high gas content area to a medium water content area, which is equivalent to the water content level of the location where well A was in the early stage of development. However, at this time, the reservoir in well B has already experienced water flooding, and the relationship between its resistivity index and water saturation conforms to the Archie model corresponding to the red fitting line in the figure. If the resistivity of the reservoir in well B at this time is R_t–B, its true water saturation is approximately S_w–B1. If the model corresponding to the blue curve is still used for the reservoir logging evaluation, the water saturation of the reservoir may be overestimated to S_w–B2, resulting in the loss of gas layers. Therefore, for the logging evaluation of reservoir saturation in oil and gas reservoirs, appropriate models and parameters need to be selected according to the development process of the oil and gas reservoirs.

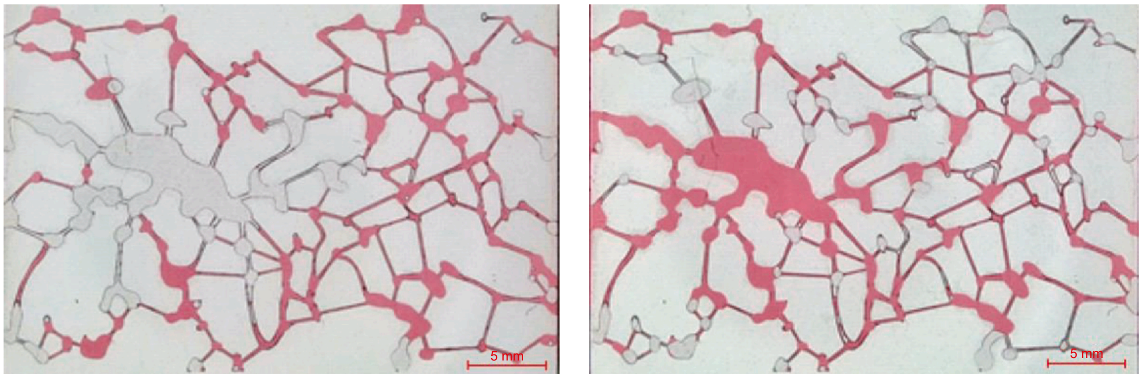

(a) S_w = 55.4% **(b)** S_w = 54.4%

Fig. 11. The distribution of pore fluids in the sample under two states with similar water saturations: **(a)** The stage of gas displacing water; **(b)** the stage of water displacing gas. The areas occupied by the red brine in the two images are comparable, but there are obvious differences in the distribution patterns.

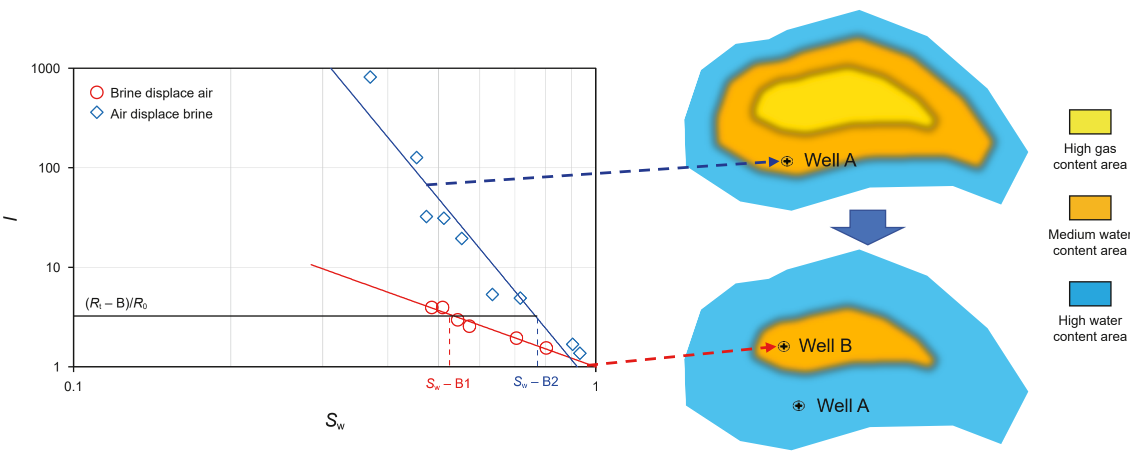

Fig. 12. Water flooding in the gas reservoir will cause changes in the relationship between the resistivity index of the reservoir and the water saturation, which in turn will affect the logging evaluation of the water saturation of the reservoir.

3.4. Limitations and future improvement directions

The above experimental results and analysis clarify the fluid seepage law and resistivity response mechanism during gas-water displacement in heterogeneous carbonate rocks, providing a basis for optimizing reservoir saturation evaluation. However, due to experimental conditions and technical constraints, this study still has certain limitations that need to be addressed. Firstly, the 2D micro-etched model simplifies the real 3D pore-throat network of carbonate rocks, failing to fully reflect the three-dimensional connectivity and spatial curvature of pores and throats, which may lead to deviations between simulated fluid flow paths and residual fluid distribution and actual reservoir conditions. Secondly, the experiment was conducted under ambient temperature and pressure, which differ significantly from the high-temperature and high-pressure environment of actual reservoirs, potentially affecting key fluid properties such as interfacial tension and viscosity, as well as the corresponding resistivity response characteristics. Additionally, the study only focused on the influence of pore structure and displacement direction, without considering the regulatory effects of factors such as rock wettability and fluid salinity, limiting the applicability of the conclusions.

To address these limitations, future experiments can be improved in the following directions: First, adopt 3D printing technology to fabricate 3D pore-throat models based on real core CT data, enhancing the authenticity of fluid displacement simulation. Second, build a high-temperature and high-pressure experimental system to simulate the actual reservoir environment and accurately capture fluid phase changes and resistivity responses under extreme conditions. Third, expand the research scope of influencing factors by introducing samples with different wettability and fluid salinity gradients to explore multi-factor coupling effects. Finally, combine experimental data with numerical simulation to establish a quantitative resistivity-saturation model considering pore structure, temperature-pressure conditions, and development stages, further improving the practical application value of the research results.

4. Conclusions

Visualized seepage experiments of gas displacing water and water displacing gas were carried out using micro-etched glass samples fabricated based on real CT images of carbonate rocks, and the fluid changes during the fluid displacement process were monitored. Based on the experimental results, the main conclusions are as follows:

(1) Owing to the strong pore structure heterogeneity of carbonate rocks, injected fluids preferentially occupy dominant seepage channels composed of large-scale pore-throats

during displacement, while residual fluids tend to be trapped in small pore-throats. Specifically, residual fluids are likely to accumulate in four types of spaces: pore - throats nearly perpendicular to dominant channels, narrow throats and their connected small pores, narrow throats parallel to large-scale pore - throats, and “sharp corner regions” within irregular pores.

(2) When a non-conductive fluid displaces a conductive fluid, the sample's resistivity exhibits a two-stage relationship with water saturation. In the early stage (water saturation >60%), non-conductive fluids only occupy large-scale pore-throats, while the conductive network formed by conductive fluids in small pore-throats remains intact, resulting in a slow increase in resistivity. In the late stage (water saturation <60%), non-conductive fluids invade small pore-throats, disrupting the conductive network and causing a sharp rise in resistivity. This two-stage pattern reduces the applicability of the simple Archie equation in strongly heterogeneous carbonate reservoirs.

(3) Even at similar water saturations, pore fluid distribution differs significantly between the gas-displacing-water and water-displacing-gas stages. During gas displacement, non-conductive gas occupies large pores and severs conductive paths, leading to higher resistivity; during water displacement, conductive brine fills large pores and forms continuous conductive paths, resulting in lower resistivity. Thus, for saturation logging evaluation of carbonate hydrocarbon reservoirs, model parameters should be adjusted based on the reservoir development stage (e.g., reservoir-forming vs. water-flooding development stages).

(4) This study has limitations: two-dimensional micro-etched models fail to accurately simulate three-dimensional pore-throat networks, and the ambient temperature and pressure conditions differ significantly from the actual high-temperature, high-pressure reservoir environment. Therefore, the findings primarily offer qualitative reference value for reservoir evaluation. In the future, we aim to upgrade experimental setups using 3D printing technology to develop three-dimensional models and enhance temperature and pressure conditions, thereby improving the authenticity of fluid displacement and resistivity responses.

CRediT authorship contribution statement

Qiang Lai: Writing – original draft. **Yu-Yu Wu:** Data curation. **Feng Wu:** Investigation. **Jiang Jia:** Methodology, Funding acquisition. **Xing-Gang Liu:** Software. **Yan-Shan Yu:** Formal analysis. **Rong Yin:** Data curation. **Li Shen:** Methodology.

Conflicts of interest

The authors declare that they have no known competing financial interests or personal relationships that could have appeared to influence the work reported in this paper.

Acknowledgments

This research was sponsored by the National Natural Science Foundation of China (No. 42304139) and the Natural Science Foundation of Sichuan Province (No. 23NSFSC6107).

References

Adebayo, A.R., Kandil, M.E., Okasha, T.M., et al., 2017. Measurements of electrical resistivity, NMR pore size and distribution, and X-ray CT-scan for performance evaluation of CO_2 injection in carbonate rocks: A pilot study. Int. J. Greenh. Gas Control 63, 1–11. https://doi.org/10.1016/j.ijggc.2017.04.016.

Al-Mahtot, O.B., 2024. Archie's parameters of a Libyan carbonate reservoirs: effect of porosity type: Case study. Arraid J. Sci. Technol. (Ajst)-Appl. Sci. Technol. 1, 39–46.

Ara, T.S., Talabani, S., Vaziri, H.H., et al., 2001. In-depth investigation of the validity of the Archie equation in carbonate rocks. In: SPE Production and Operations Symposium, SPE-67204-MS. https://doi.org/10.2118/67204-MS.

Archie, G.E., 1942. The electrical resistivity log as an aid in determining some reservoir characteristics. Trans. Aime 146, 54–62.

Baban, A., Hosseini, M., Keshavarz, A., et al., 2024. Robust NMR examination of the three-phase flow dynamics of carbon geosequestration combined with enhanced oil recovery in carbonate formations. Energy Fuel. 38 (3), 2167–2176. https://doi.org/10.1021/acs.energyfuels.3c04674.

Cai, J., Wei, W., Hu, X., et al., 2017. Electrical conductivity models in saturated porous media: a review. Earth Sci. Rev. 171, 419–433. https://doi.org/10.1016/j.earscirev.2017.06.013.

Elkatatny, S., Mahmoud, M., Tariq, Z., et al., 2018. New insights into the prediction of heterogeneous carbonate reservoir permeability from well logs using artificial intelligence network. Neural Comput. Appl. 30 (9), 2673–2683. https://doi.org/10.1007/s00521-017-2850-x.

Gogoi, S., Gogoi, S.B., 2019. Review on microfluidic studies for EOR application. J. Pet. Explor. Prod. Technol. 9 (3), 2263–2277. https://doi.org/10.1007/s13202-019-0610-4.

Guo, J., Ling, Z., Xu, X., et al., 2023. Saturation determination and fluid identification in carbonate rocks based on well logging data: A middle eastern case study. Processes 11 (4), 1282. https://doi.org/10.3390/pr11041282.

Han, Y., Zhou, C., Yu, J., et al., 2019. Experimental investigation on the effect of wettability on rock-electricity response in sandstone reservoirs. Fuel 239, 1246–1257. https://doi.org/10.1016/j.fuel.2018.11.072.

Hao, Y., Li, Z., Su, Y., et al., 2022. Experimental investigation of CO_2 storage and oil production of different CO_2 injection methods at pore-scale and core-scale. Energy 254, 124349. https://doi.org/10.1016/j.energy.2022.124349.

Harju, J.A., Malki, M.L., Rabiei, M., et al., 2023. Log scale rock physics modelling to study the effect of mineralogy on elastic properties of the Bakken Formation. Geoenergy Sci. Eng. 223, 211432. https://doi.org/10.1016/j.geoen.2023.211432.

He, J., Li, M., Zhou, K., et al., 2020. Effects of vugs on resistivity of vuggy carbonate reservoirs. Petrol. Explor. Dev. 47 (3), 527–535. https://doi.org/10.1016/S1876-3804(20)60070-2.

Ho, T.M., Yang, J., Tsai, P.A., 2021. Microfluidic mass transfer of CO_2 at elevated pressures: implications for carbon storage in deep saline aquifers. Lab Chip 21 (20), 3942–3951. https://doi.org/10.1039/D1LC00106J.

Hosseini, M., 2016. Estimation of mean pore-size using formation evaluation and Stoneley slowness. J. Nat. Gas Sci. Eng. 33, 898–907. https://doi.org/10.1016/j.jngse.2016.06.029.

Hosseini, M., Ali, M., Fahimpour, J., et al., 2023. Calcite-fluid interfacial tension: H_2 and CO_2 geological storage in carbonates. Energy Fuel. 37 (8), 5986–5994. https://doi.org/10.1021/acs.energyfuels.3c00399.

Hosseini, M., Ali, M., Fahimpour, J., et al., 2024. Energy storage in carbonate and basalt reservoirs: investigating secondary imbibition in H_2 and CO_2 systems. Adv Geo-Energy Res 11 (2), 132–140. https://doi.org/10.46690/ager.2024.02.05.

Jia, J., Ke, S., Li, J., et al., 2020. Estimation of permeability and saturation based on imaginary component of complex resistivity spectra: A laboratory study. Open Geosci. 12 (1), 299–306. https://doi.org/10.1515/geo-2020-0108.

Jia, J., Ke, S., Rezaee, R., et al., 2021. The frequency exponent of artificial sandstone's complex resistivity spectrum. Geophys. Prospect. 69 (4), 856–871. https://doi.org/10.1111/1365-2478.13072.

Jia, J., Zhao, J., Jiao, S., et al., 2022. Multi-point resistivity measurement system for full-diameter long cores during fluid displacement. Rev. Sci. Instrum. 93 (12). https://doi.org/10.1063/5.0131486.

Kolawole, O., Millikan, C., Kumar, M., et al., 2022. Impact of microbial-rock-CO_2 interactions on containment and storage security of supercritical CO_2 in carbonates. Int. J. Greenh. Gas Control 120, 103755. https://doi.org/10.1016/j.ijggc.2022.103755.

Li, J., Ke, S., Yin, C., Kang, Z., Jia, J., Ma, X., 2019. A laboratory study of complex resistivity spectra for predictions of reservoir properties in clear sands and shaly sands. J. Pet. Sci. Eng. 177, 983. https://doi.org/10.1016/j.ijggc.2022.103755.

Liang, B., Chen, C., Jia, C., et al., 2024. Carbon capture, utilization and storage (CCUS) in oil and gas reservoirs in China: Status, opportunities and challenges. Fuel 375, 132353. https://doi.org/10.1016/j.fuel.2024.132353.

Liu, Z., McClure, J.E., Armstrong, R.T., 2018. Influence of wettability on phase connectivity and electrical resistivity. Phys. Rev. E. 98 (4), 43102. https://doi.org/10.1103/PhysRevE.98.043102.

Lu, H., Huang, F., Jiang, P., et al., 2021. Exsolution effects in CO_2 huff-n-puff enhanced oil recovery: Water-Oil-CO_2 three phase flow visualization and measurements by micro-PIV in micromodel. Int. J. Greenh. Gas Control 111, 103445. https://doi.org/10.1016/j.ijggc.2021.103445.

Malki, M.L., Saberi, M.R., Kolawole, O., et al., 2023. Underlying mechanisms and controlling factors of carbonate reservoir characterization from rock physics

perspective: A comprehensive review. Geoenergy Sci. Eng. 226, 211793. https://doi.org/10.1016/j.geoen.2023.211793.
Mohammadi, M., Niri, M.E., Bahroudi, A., et al., 2025. A novel electrical rock typing approach to improve estimating formation resistivity factor in carbonate rocks. J. Pet. Explor. Prod. Technol. 15 (1), 7. https://doi.org/10.1007/s13202-024-01920-6.
Nepal, A., Hidalgo, J.J., Ortín, J., et al., 2025. Mechanisms of interface jumps, pinning and hysteresis during cyclic fluid displacements in an isolated pore. J. Colloid Interface Sci. 695, 137767. https://doi.org/10.1016/j.jcis.2025.137767.
Prakoso, S., Burhannudinnur, M., Herdiansyah, F., et al., 2025. Assessing pore quality impact on saturation exponent and water saturation calculation. J. Pet. Explor. Prod. Technol. 15 (8), 129. https://doi.org/10.1007/s13202-025-02028-1.
Qian, C., Rui, Z., Liu, Y., et al., 2025. Microfluidic investigation on microscopic flow and displacement behavior of CO_2 multiphase system for CCUS-EOR in heterogeneous porous media. Chem. Eng. J. 505, 159135. https://doi.org/10.1016/j.cej.2024.159135.
Revil, A., Ahmed, A.S., Matthai, S., 2018. Transport of water and ions in partially water-saturated porous media. Part 3. Electrical conductivity. Adv. Water Resour. 121, 97–111. https://doi.org/10.1016/j.advwatres.2018.08.007.
Sharbatian, A., Abedini, A., Qi, Z., et al., 2018. Full characterization of CO_2-oil properties on-chip: Solubility, diffusivity, extraction pressure, miscibility, and contact angle. Anal. Chem. 90 (4), 2461–2467. https://doi.org/10.1021/acs.analchem.7b05358.
Wang, Y., Lei, Z., Sun, L., et al., 2024. Study on the minimum miscibility pressure and phase behavior of CO_2-shale oil in nanopores. Chem. Eng. J. 497, 154493. https://doi.org/10.1016/j.cej.2024.154493.
Wu, F., Yao, C., Cong, L., et al., 2020. Pore-scale gas-water flow in rock: Visualization experiment and simulation. Open Geosci. 12 (1), 532–546. https://doi.org/10.1515/geo-2020-0105.
Xu, R., Li, R., Ma, J., et al., 2017. Effect of mineral dissolution/precipitation and CO_2 exsolution on CO_2 transport in geological carbon storage. Accounts Chem. Res. 50 (9), 2056–2066. https://doi.org/10.1021/acs.accounts.6b00651.
Xu, Z., Li, S., Li, B., et al., 2020. A review of development methods and EOR technologies for carbonate reservoirs. Pet. Sci. 17 (4), 990–1013. https://doi.org/10.1007/s12182-020-00467-5.
Yang, L.I., Zhijiang, K., Zhaojie, X., et al., 2018. Theories and practices of carbonate reservoirs development in China. Petrol. Explor. Dev. 45 (4), 712–722. https://doi.org/10.1016/S1876-3804(18)30074-0.
Zhang, P., Pan, B., Guo, Y., et al., 2025. Study on an improved saturation parameter method based on joint inversion of NMR and resistivity data in porous media. Pet. Sci. 22 (6), 2312–2324. https://doi.org/10.1016/j.petsci.2025.03.024.
Zhang, X., Su, Y., Li, L., et al., 2022. Microscopic remaining oil initiation mechanism and formation damage of CO_2 injection after waterflooding in deep reservoirs. Energy 248, 123649. https://doi.org/10.1016/j.energy.2022.123649.
Zhao, G., An, J., Zhu, H., et al., 2025a. Characteristics of medium resistivity response during the water–oil displacement process. Water 17 (7), 1090. https://doi.org/10.3390/w17071090.
Zhao, J., Lin, Z., Tang, D., et al., 2025b. Saturation model for pore-type gas hydrate based on additional muddy conductive digital core. J. Geophys. Eng. 22 (1), 165–178. https://doi.org/10.1093/jge/gxae115.